Chinese Chemical Letters 33 (2022) 3739–3744

Contents lists available at ScienceDirect

Chinese Chemical Letters

journal homepage: www.elsevier.com/locate/cclet

Doping transition metal in $PdSeO_3$ atomic layers by aqueous cation exchange: A new doping protocol for a new 2D photocatalyst

Xiuming Zhang, Rongrong Pan, Tailei Hou, Shuping Zhang, Xiaodong Wan, Yuemei Li, Shan Liu, Jia Liu*, Jiatao Zhang*

Beijing Key Laboratory of Construction-Tailorable Advanced Functional Materials and Green Applications, Experimental Center of Advanced Materials, School of Materials Science & Engineering, Beijing Institute of Technology, Beijing 100081, China

ARTICLE INFO

Article history:
Received 30 August 2021
Revised 12 October 2021
Accepted 29 October 2021
Available online 5 November 2021

Keywords:
2D Semiconductor
Atomic layers
Photocatalysis
Doping
Cation exchange

ABSTRACT

Elemental doping confined in atomically-thin 2D semiconductors offers a compelling strategy for constructing high performance photocatalysts. Although impressive progress has been achieved based on co-thermolysis method, the choices of dopants as well as semiconductor hosts are still quite limited to yield the elaborate photocatalyst with atomic-layer-confined doping defects, owing to the difficulty in balancing the reaction kinetics of different precursors. This study shows that the cation exchange reaction, which is dictated by the Pearson's hard and soft acids and bases (HSAB) theory and allowed to proceed at mild temperatures, can be developed into a conceptually new protocol for engineering elemental doping confined in semiconductor atomic layers. To this aim, the two atomic layers of a new type of 2D photocatalyst $PdSeO_3$ ($PdSeO_3$ 2ALs, 1.1 nm) are created by liquid exfoliation and exploited as a proof-of-concept prototype. It is demonstrated that the Mn(II) dopants with controlled concentrations can be incorporated into $PdSeO_3$ 2ALs *via* topological Mn^{2+}-for-Pd^{2+} cation exchange performed in water/isopropanol solution at 30 °C. The resulting Mn-doped $PdSeO_3$ 2ALs present enhanced capacity for driving photocatalytic oxidation reactions in comparison with their undoped counterparts. The findings here suggest that the new route mediated by post synthetic cation exchange promises to give access to manifold 2D confined-doping photocatalysts, with little perturbations on the thickness, morphology, and crystal structure of the atomically-thin semiconductor hosts.

Given its significant impact on modulating the electronic structure of semiconductors, elemental doping has been widely demonstrated to be a viable tool for optimizing the functions of semiconductor-based photocatalysts [1–7]. This is especially pertinent to the two-dimensional (2D) atomically-thin semiconductors, where the dopants are primarily exposed on the surface and therefore can inhibit the adverse effects associated with doping such as forming recombination centers in the interior of bulk semiconductors [8–12]. In the last decade, the Rh-doped Ca-Nb-O [13], Co-doped In_2S_3 [14], Ru-doped TiO_2 [15], Pt or B-doped g-C_3N_4 2D layers [16], *etc.*, have well exemplified their great advantages in photocatalytic process with expanded light absorption range, enhanced charge separation and promoted surface redox reaction. Despite much promise, however, the study in this area is hindered by the limited capability to construct such atomic-layer-confined doping systems. This is because currently, dopant incorporation into semiconductor 2D layers is primarily implemented by co-thermolysis of mixed precursors at high temperatures [17,18]. The rigorous requirement on balancing the relative chemical reactivity of different precursors causes finite choice of available host semiconductors and the types of dopants. Besides, during the co-thermolysis process, the existence of foreign dopants often significantly affects the nucleation and growth mechanism of the host semiconductors, detrimental to keeping the integrity of the atomic-layer structure or leading to unsuccessful doping [19,20]. Therefore, there is an urgent need to develop alternative synthetic strategies for engineering doping in 2D semiconductor photocatalysts.

On the other hand, cation exchange has recently emerged as a powerful means to tailor semiconductor nanocrystals *via* versatile composition tuning with morphology retention. In fact, based

* Corresponding authors.
E-mail addresses: liujia86@bit.edu.cn (J. Liu), zhangjt@bit.edu.cn (J. Zhang).

https://doi.org/10.1016/j.cclet.2021.10.088
1001-8417/

on cation exchange, a new chemical route has been established for realizing controllable doping in semiconductor nanocrystals and quantum dots in order to regulate their optoelectronic or magnetic properties [21–25]. However, these progresses are mainly restricted to chalcogenide (II-VI) and nitride (III-V) semiconductors. Although efforts have been devoted to expanding the applicability of cation exchange, to date such synthetic strategy has achieved limited success in creation of doped oxides and other types of semiconductors (such as doped oxysulfides and oxyselenides). Moreover, cation exchange reactions are generally performed in organic phase involving the use of ligands with long alkyl tails like oleylamine, oleic acid, dodecanethiol, *etc.* [19,24,26-28]. Thus resulting semiconductor nanocrystals confront obstacles to forming uniform dispersion in aqueous solution and to catalyzing chemical reactions because of blocked surface sites [29]. As a consequence, cation exchange, though has manifested great potentials in creation of elaborate doped systems toward applications in displays and solid-state lighting, to the best of our knowledge, has seldom been exploited to manipulate elemental doping in photocatalyst materials.

Herein, we demonstrate that aqueous cation exchange can constitute a facile and reliable way for modulating cation doping confined in semiconductor atomic layers to ameliorate their photocatalytic behaviors. As a proof-of-concept prototype, $PdSeO_3$ atomic layers, which have been proposed to be a highly promising photocatalyst for overall water splitting based on density functional theory (DFT) calculations [30], were fabricated and employed as the host materials. Our results demonstrated that different amount of Mn(II) dopants can be incorporated into $PdSeO_3$ atomic layers (thickness of 1.1 nm, corresponding to two atomic layers) *via* cation exchange performed in aqueous solution at mild temperature (30 °C). The obtained Mn-doped $PdSeO_3$ photocatalyst well retained their atomic layer morphology and high crystallinity. With increasing the Mn dopant concentration, the valance band (VB) maximum of $PdSeO_3$ atomic layers was gradually down-shifted, indicative of the enhanced oxidation capability for photogenerated holes. Furthermore, we found that the presence of Mn dopants in $PdSeO_3$ atomic layers lead to accelerated organics degradation rate under visible light irradiation, contributed by the promoted generation of reactive oxygen species (ROS) such as hydroxyl radicals (•OH). On the basis of these findings, we envision that cation exchange can be developed into an important synthetic approach for elaborate construction and manipulation of doping defects in 2D photocatalysts.

In this work, as illustrated in Fig. 1a, we demonstrate a feasible cation exchange strategy for fabricating the 2D $PdSeO_3$ atomic layers doped with transition-metal Mn(II) ions, where the morphology and crystal structure of pristine $PdSeO_3$ are almost unaffected during the ion exchange process. $PdSeO_3$ is a new emerging 2D photocatalyst that has been theoretically predicted to be suitable for splitting water into H_2 an O_2 under visible light irradiation. In our prior research, we have conducted the first experimental study on the ultrathin $PdSeO_3$ nanosheets that were synthesized through the quaternary ammonium intercalation-assisted electrochemical exfoliation method [31]. The resultant $PdSeO_3$ nanosheets possessed a thickness of 4–5 nm, corresponding to the stacking of 7 atomic layers of $PdSeO_3$ slab. Although such ultrathin 2D photocatalyst showed excellent photocatalytic hydrogen evolution activity, it was failed to drive the water oxidation half reaction, at variance with the DFT predictions for $PdSeO_3$ monolayers. Therefore, to optimize the photocatalytic function of $PdSeO_3$ photocatalyst, it is desirable to further reduce the layer thickness and exploit the doping strategy to enhance its oxidation ability.

To this end, one of our aims in this work is to develop an alternative synthetic approach for creation of the $PdSeO_3$ atomic layers with even reduced thickness. According to previous report,

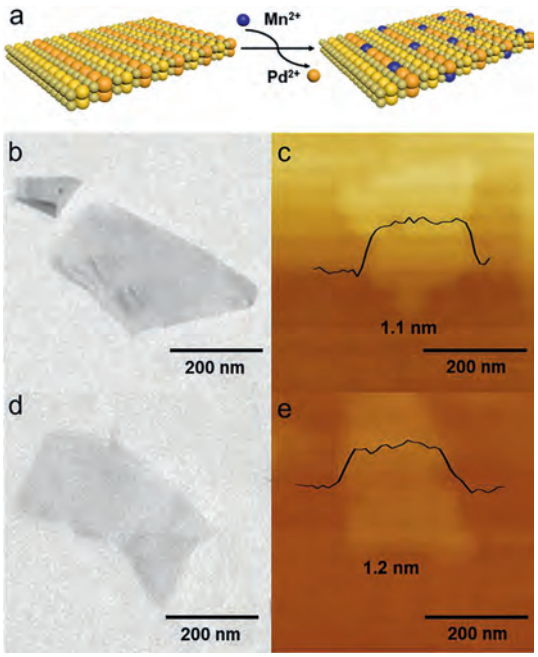

Fig. 1. (a) Schematic illustration of doping transition metal ions Mn^{2+} into $PdSeO_3$ 2ALs through cation exchange reaction. (b) TEM image and (c) AFM image of $PdSeO_3$ 2ALs; (d) TEM image and (e) AFM image of Mn(3)-$PdSeO_3$ 2ALs.

as the surface tension of graphite was well matched with the isopropanol/water (1:1) solution, high quality and yield graphene could be successfully synthesized in isopropanol/water (1:1) solution under ultrasonic treatment [32]. In view of the similar cleavage energy of $PdSeO_3$ monolayer to that of graphene [30], here sonication-assisted exfoliation in isopropanol/water (1:1) solution was applied to exfoliate the bulk $PdSeO_3$ crystals into atomic layers. This generated a light-orange-colored solution, which was highly stable and exhibited a distinct Tyndall effect. No precipitations were observed even after being stored for 2 weeks under ambient conditions, reflecting the well retained colloidal state of the as-exfoliated $PdSeO_3$ (Fig. S1 in Supporting information). As shown in Fig. 1b, transmission electron microscopic (TEM) image of the as-exfoliated $PdSeO_3$ indicates its uniform freestanding and large-area sheet-like morphology with a lateral size of *ca.* 200 nm. The atomic force microscopic (AFM) image in Fig. 1c discloses that the resulting $PdSeO_3$ layer possesses an average thickness of 1.1 nm, which is consistent with two atomic layers (2ALs) of $PdSeO_3$ slab along the z direction. The above results demonstrate that the $PdSeO_3$ 2ALs can be readily accessed by sonication-assisted exfoliation in proper solvent.

Based on the Pearson's hard and soft acids and bases (HSAB) theory, the coordination ability of tributylphosphine (TBP, soft base) with Pd^{2+} (soft acid, hardness of 6.75) is stronger than that of Mn^{2+} (hard acid, hardness of 9.02) [33–35]. Therefore, when TBP ligands and Mn^{2+} cations are both introduced into the colloidal suspension of $PdSeO_3$ 2ALs, a certain amount of Pd^{2+} would be dragged out from the lattice of $PdSeO_3$ by the TBP ligand and replaced with the guest Mn^{2+} ions. In view of this, we performed the Mn^{2+}-for-Pd^{2+} cation exchange reaction on $PdSeO_3$ 2ALs in isopropanol/water (1:1) mixture at 30 °C. The resultant samples are denoted as Mn(X)-$PdSeO_3$ 2ALs, where X (X% = 0.75%, 1.5%, 3% and 6%) represents the theoretical percentage of Mn/Pd molar ratio during synthesis. As shown in Fig. S2 (Supporting information), the concentration of Mn dopants in Mn(X)-$PdSeO_3$ 2ALs was measured at 0.6%, 0.75%, 1.4% and 1.5% when increasing the Mn/Pd molar ratio from 0.75% to 1.5%, 3% and 6%, correspondingly.

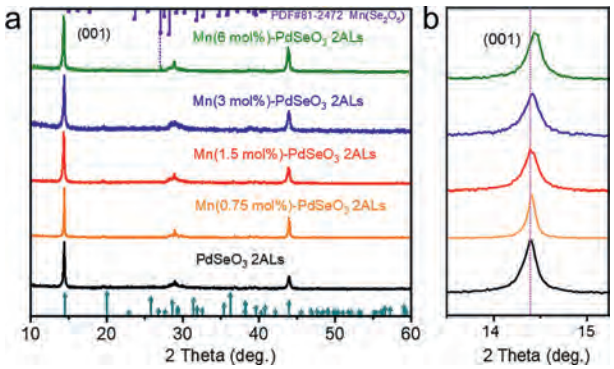

Fig. 2. (a) XRD patterns of pristine $PdSeO_3$ 2ALs and Mn(X)-$PdSeO_3$ 2ALs with different dopant concentrations. (b) The detailed analysis of XRD patterns shows gradual shift of the (001) diffraction peak after cation exchange reaction with increased concentration of Mn^{2+} dopants.

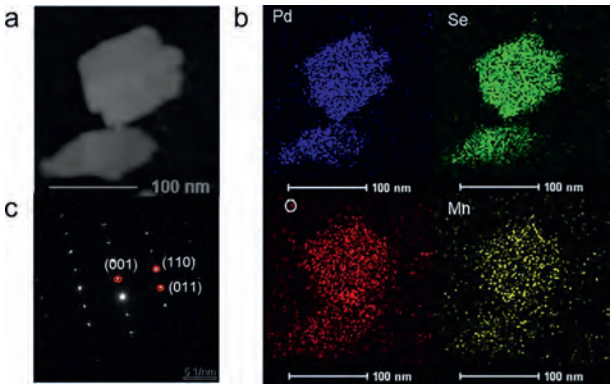

Fig. 3. (a) HAADF-STEM image of an individual sheet of Mn(3)-$PdSeO_3$ 2ALs, (b) the corresponding EDS elemental maps for Pd, Se, O, and Mn, and (c) the corresponding SAED pattern.

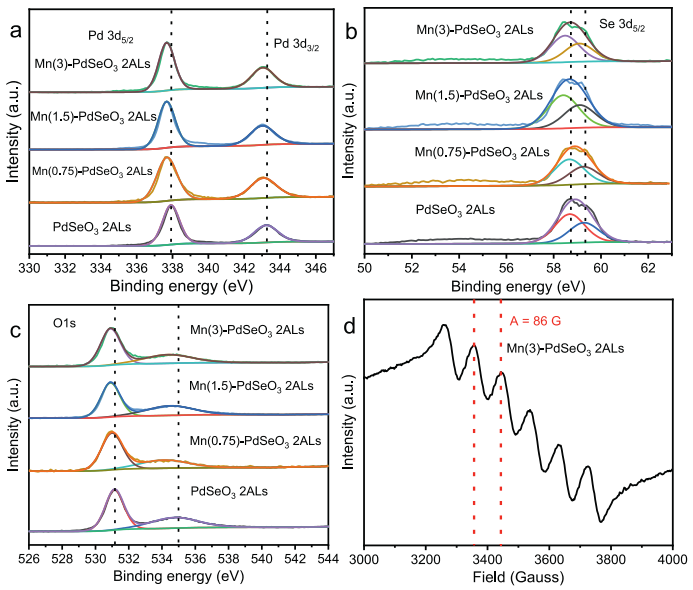

Fig. 4. High-resolution (a) Pd 3d, (b) Se 3d, and (c) O 1s XPS spectra for $PdSeO_3$ 2ALs and Mn(X)-$PdSeO_3$ 2ALs. (d) X-band EPR spectrum of Mn(3)-$PdSeO_3$ 2ALs at room temperature.

As indicated by the TEM image of Mn(3)-$PdSeO_3$ 2ALs in Fig. 1d, the cation exchange reaction dose not obviously affect the morphology of the sample. The corresponding AFM image in Fig. 1e reveals that the ultrathin feature of the exfoliated $PdSeO_3$ 2ALs is well kept after the cation exchange process (thickness of 1.2 nm for Mn(3)-$PdSeO_3$ 2ALs). It was found that the suspension of Mn(X)-$PdSeO_3$ 2ALs was highly stable over several days, inferring the colloidal state of the sample was little perturbed under the exchange reaction condition. The X-ray diffraction (XRD) patterns of $PdSeO_3$ 2ALs before and after cation exchange are presented in Fig. 2a. One can see that all the samples are highly crystallined showing diffraction peaks coincided well with the crystallographic data reported for $PdSeO_3$, expect for Mn(6)-$PdSeO_3$ 2ALs which additionally exhibits the characteristic peak of $MnSe_2O_5$ (JCPDS card No. 81–2472, thus in the following studies this sample will not be further discussed due to the presence of impurity). Careful examination of the XRD patterns further uncovers that the (001) peaks of Mn(X)-$PdSeO_3$ 2ALs are monotonically shifted to higher angles with increasing the dopant concentration (Fig. 2b). This is consistent with lattice contraction caused by the substitution of Pd^{2+} by Mn^{2+} with smaller ionic radius. The high-angle annular dark-field scanning transmission electron microscopy (HAADF-STEM) and the associated energy-dispersive X-ray spectroscopy (EDX) elemental analyses demonstrate that the elements of Pd, Se, O, and Mn are uniformly distributed within the Mn(3)-$PdSeO_3$ 2ALs atomic layers (Figs. 3a and b). From Fig. 3c, the selected area electron diffraction (SAED) pattern collected from an individual nanosheet of Mn(3)-$PdSeO_3$ 2ALs clearly reveals its single crystallined nature, in good agreement with the XRD result.

The chemical state of the elements in $PdSeO_3$ and Mn(X)-$PdSeO_3$ 2ALs was analyzed by X-ray photoelectron spectroscopy (XPS). For pristine $PdSeO_3$ 2ALs, the high-resolution XPS spectrum of Pd 3d (Fig. 4a) shows two bands at 343.2 and 337.8 eV, corresponding to Pd^{2+} $3d_{3/2}$ and Pd^{2+} $3d_{5/2}$, respectively [28]. It can be seen obviously that after the cation exchange reaction, the binding energies of Pd 3d are decreased with the increment of Mn dopant concentration, which can be well rationalized by the changed electronic environment as a result of the incorporation of Mn into $PdSeO_3$ [36–39]. Similar phenomena are discernible for the high-resolution XPS spectra of Se 3d and O 1s (Figs. 4b and c), where the characteristic peaks assigned to Se^{4+} and O^{2-} in Mn(X)-$PdSeO_3$ 2ALs are shifted to lower binding energies in comparison with pristine $PdSeO_3$ 2ALs. These observations strongly suggest the occurrence of cations substitution in $PdSeO_3$ 2ALs after the exchange reaction. More importantly, we exploited the electron paramagnetic resonance (EPR) measurement, which is a vital tool for detecting the valence state and distribution of transition metals in nanomaterials, to provide direct evidence for the existence of Mn^{2+}dopants in Mn(X)-$PdSeO_3$ 2ALs. As shown in Fig. 4d, the EPR signal for Mn(3)-$PdSeO_3$ 2ALs manifests six equally spaced lines showing an equal intensity (with hyperfine coupling constant, at $A = 86$ G). Such observation is exactly the same as those reported for Mn-doped nanocrystals, which unambiguously verifies the residence of Mn^{2+} dopants inside the atomically-thin $PdSeO_3$ host with a homogeneous distribution (in other words, the Mn^{2+} species are not adsorbed on the surface of $PdSeO_3$ 2ALs, and are not clustered together) [40,41].

It is well-known that doping would affect the band structure of semiconductors and consequently influences their photocatalytic activities. UV–vis absorption spectra in Fig. 5a demonstrate that the band gap of the Mn(X)-$PdSeO_3$ 2ALs samples are all around 2.59 eV, which is slightly smaller than that of pristine $PdSeO_3$ 2ALs (2.71 eV), indicative of the enhanced capacity for harvesting visible light [42]. Besides, the valence band (VB) position of the samples was determined by the XPS valence band spectra as shown in Fig. 5b. The pristine $PdSeO_3$ 2ALs display a VB maximum edge at

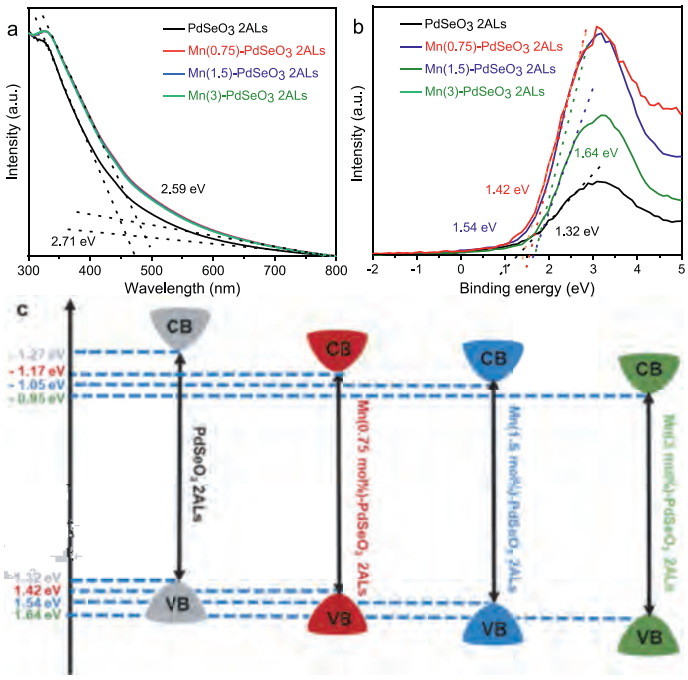

Fig. 5. (a) UV–vis absorption spectra of $PdSeO_3$ 2ALs and Mn(X)-$PdSeO_3$ 2ALs. (b) Valence-band XPS spectra of $PdSeO_3$ 2ALs and Mn(X)-$PdSeO_3$ 2AL. (c) Schematic illustration of the band structures determined for $PdSeO_3$ 2ALs and Mn(X)-$PdSeO_3$ 2ALs.

1.32 V, while for the Mn(X)-$PdSeO_3$ 2ALs samples, their VB maximum edges are gradually down-shifted with increasing the concentration of Mn^{2+} dopants. These results suggest that the introduction of Mn^{2+} into $PdSeO_3$ 2ALs is beneficial for improving the oxidation ability of the photogenerated holes [43]. The band structures for each sample are depicted in Fig. 5c. Especially, for Mn(3)-$PdSeO_3$ 2ALs, its VB and conduction band (CB) edges are at 1.64 and −0.95 V, respectively, which is thermodynamically capable of driving overall water splitting reaction.

Encouraged by the theoretical studies predicting that $PdSeO_3$ layers can function as a promising water splitting photocatalyst [30], we first conducted photocatalytic overall water splitting reaction in pure water under visible light irradiation. However, it was found that no H_2 or O_2gasses were evolved from the reaction system for both $PdSeO_3$ and Mn(3)-$PdSeO_3$ 2ALs (Fig. S3 in Supporting information). Even with the assistance of electron sacrificial reagents like $AgNO_3$ and $NaIO_3$, these two samples still cannot generate O_2 *via* photocatalytic water oxidation reaction (Fig. S4 in Supporting information). We further carried out electrocatalytic oxygen evolution reaction (OER) in 1 mol/L KOH electrolyte to evaluate the intrinsic water oxidation ability of the samples. As indicated by the polarization curves in Fig. S5 (Supporting information), the pristine $PdSeO_3$ 2ALs require an overpotential of 1.38 V (*vs.* RHE) at the current density of 10 mA/cm^2, while Mn(3)-$PdSeO_3$ 2ALs can reach the current density of 10 mA/cm^2 with an overpotential of 1.27 V (*vs.* RHE). Such large overpotential values are close to that reported for g-C_3N_4 of 1.56 V [44], unfavorable for the proceeding of water oxidation half reaction. However, the reduced overpotential (110 mV) observed for Mn(3)-$PdSeO_3$ 2ALs relative to $PdSeO_3$ 2ALs evidences that doping of Mn^{2+} into $PdSeO_3$ indeed can improve the oxidation ability of the catalyst.

Photocatalytic degradation of organic dyes or toxic pollutants is of great significance in environmental pollutant treatment [45,46]. Metronidazole (MTZ) is a commonly used antibiotic drug, however its entry into water can cause great damage to environment and ultimately endanger human health [47,48]. In this study MTZ was employed as the probe molecule to evaluate the performance of $PdSeO_3$ and Mn(3)-$PdSeO_3$ 2ALs in photocatalytic degradation reaction under visible light irradiation ($\lambda > 420$ nm). As shown in Figs. 6a and b, during the reaction the characteristic absorption peak of MTZ at 318 nm was gradually disappeared and blue-shifted, indicating the degradation of MTZ into new substances with the presence of catalysts under visible light. Fig. 6c shows the comparison of the photocatalytic degradation curves for the two samples (the blank measurement with absence of catalyst is also exhibited as a reference). After 120 min of irradiation, the removal ratio of MTZ was only 45% for $PdSeO_3$ 2ALs. However, Mn(3)-$PdSeO_3$ 2ALs exhibited significantly enhanced photocatalytic activity with removal ratio of MTZ up to 85% in the same time period. The photocatalytic decomposition kinetics of MTZ are further plotted as presented in Fig. 6d, which corroborate that the photocatalytic processes are all well fitted with the first-order reaction dynamic model (Eq. 1):

$$-\ln(C/C_0) = kt \quad (1)$$

where C_0 is the MTZ concentration after 30 min of stirring in dark, while C and k are the temporal concentration of MTZ at reaction time t and the degradation rate constant, respectively. For Mn(3)-$PdSeO_3$ 2ALs, its kinetic constant k was up to 0.016 min^{-1}, which was about 2 times higher than that of $PdSeO_3$ 2ALs (0.007 min^{-1}), clearly substantiating the beneficial effect brought about by Mn^{2+} doping into $PdSeO_3$ 2ALs.

The hydroxyl radicals ($^{\bullet}OH$) and superoxide radicals ($^{\bullet}O_2^-$) as highly reactive oxygen species (ROS) play an important role in photocatalytic degradation reactions. In order to investigate the photocatalytic degradation mechanism, the spin-trapping electron spin resonance (ESR) measurements were conducted to probe the generation of $^{\bullet}OH$ and $^{\bullet}O_2^-$ species during the photocatalytic reaction. As displayed in Fig. 7a, no signals for $^{\bullet}OH$ were detected under dark conditions. However, when the sample was irradiated with visible light, the four characteristic peaks for DMPO-$^{\bullet}OH$ were detected immediately for both $PdSeO_3$ and Mn(3)-$PdSeO_3$ 2ALs. The signal intensities of Mn(3)-$PdSeO_3$ 2ALs were obviously much stronger than those of $PdSeO_3$ 2ALs, suggesting that a higher amount of $^{\bullet}OH$ radicals were produced on the surface of Mn(3)-$PdSeO_3$ 2ALs. This is in good accordance with the conclusion that Mn^{2+} doping can markedly enhance the oxidation ability of $PdSeO_3$ 2ALs. With regard to the $^{\bullet}O_2^-$ radicals, similar observations were found indicative of the presence of $^{\bullet}O_2^-$ radicals during photocatalytic reaction and their higher production efficiency on Mn(3)-$PdSeO_3$ 2ALs (Fig. 7b). The promoted generation of both $^{\bullet}OH$ and $^{\bullet}O_2^-$ species on Mn(3)-$PdSeO_3$ 2ALs can largely contribute to boosting the degradation process of MTZ under visible light. Besides, the photoelectrochemical (PEC) currents and electrochemical impedance spectroscopy (EIS) Nyquist plots were also compared for $PdSeO_3$ and Mn(3)-$PdSeO_3$ 2ALs (Figs. 7c and d). The results demonstrate that doping of Mn^{2+} can improve separation of photogenerated charge carriers and facilitate their transfer through the solid/liquid interface, additionally conducive to photocatalytic degradation of MTZ.

In summary, two atomic layers of $PdSeO_3$ are firstly created through a facile exfoliation method by matching the surface tension components between material and solvent. The resultant $PdSeO_3$ 2ALs afford a new prototype for promising 2D photocatalyst and based on which, we demonstrate that aqueous cation exchange at ambient temperature can be utilized to realize confined doping of Mn(II) into the atomically-thin 2D photocatalysts with well-preserved thickness, morphology and crystal structure. We further show that programmable enhancement in the oxidation ability of Mn-doped $PdSeO_3$ 2ALs is achievable by raising the Mn(II) dopant concentration, in view of the downward-shifted VB

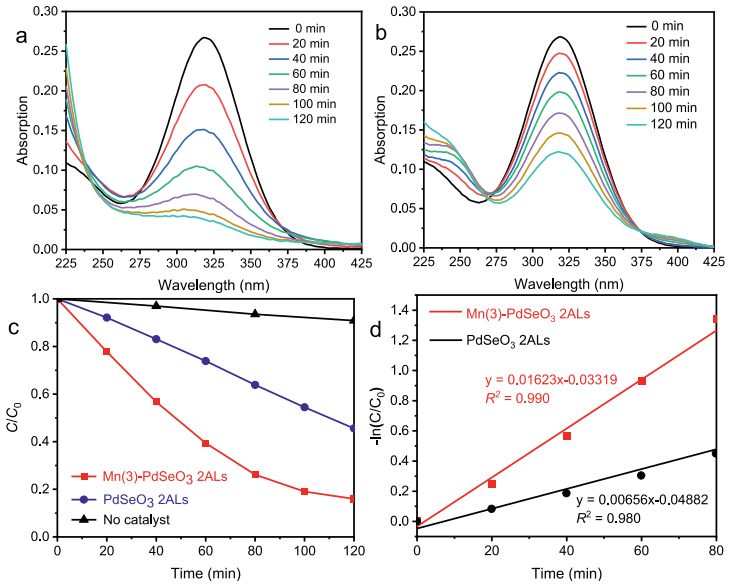

Fig. 6. The evolution of UV–vis absorption spectra of MTZ solution under visible light irradiation in presence of (a) Mn(3)-$PdSeO_3$ 2ALs and (b) $PdSeO_3$ 2ALs. (c) Photocatalytic degradation curves of MTZ with (blue line for $PdSeO_3$ 2ALs; red line for Mn(3)-$PdSeO_3$ 2ALs) or without catalysts (black line) under visible light irradiation. (d) The kinetics of MTZ photocatalytic degradation over $PdSeO_3$ 2ALs and Mn(3)-$PdSeO_3$ 2ALs.

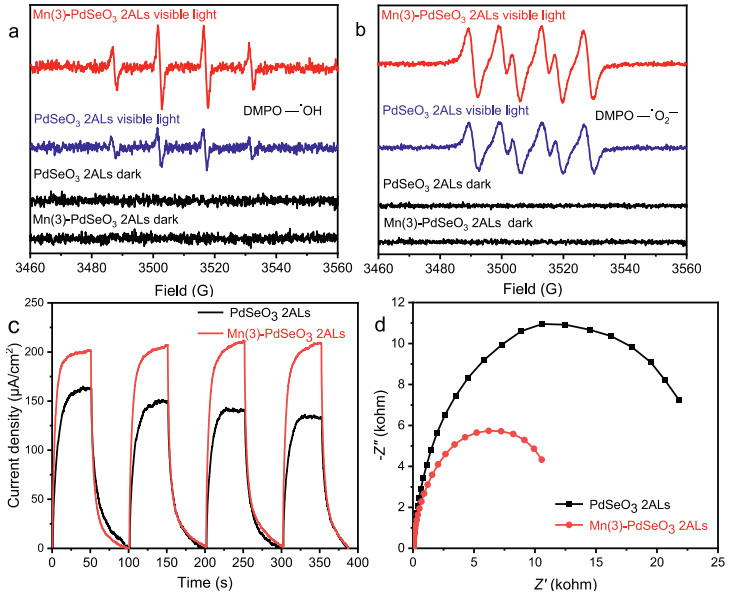

Fig. 7. DMPO spin-trapping ESR spectra for detecting the *in situ* formed (a) ·OH and (b) $\cdot O_2^-$ radicals over $PdSeO_3$ 2ALs and Mn(3)-$PdSeO_3$ 2ALs before and after irradiation by visible light for 5 min. (c) Photocurrent density-time curves and (d) EIS Nyquist plots for $PdSeO_3$ 2ALs and Mn(3)-$PdSeO_3$ 2ALs.

edges, the reduced OER overpotentials and the promoted generation of ·OH radicals under visible light irradiation. These advantages make the Mn-doped $PdSeO_3$ 2ALs display a much higher rate for photocatalytic degradation of metronidazole in comparison with the undoped $PdSeO_3$ 2ALs. Our results strongly indicate that distinct from the co-thermolysis processes, the HSAB theory-directed cation exchange can offer a conceptually new protocol for manipulating elemental doping confined in atomic-layered 2D photocatalysts. This may open up new possibilities for creating a large variety of atomic-layer-confined doping photocatalyst systems and help to deepen the insights into the role of atomic structure of doping defects on photocatalytic properties.

Declaration of competing interest

The authors declare that they have no known competing financial interests or personal relationships that could have appeared to influence the work reported in this paper.

Acknowledgments

This work was supported by the National Natural Science Foundation of China (Nos. 52072035, 51631001, 21801015, 51702016, 51902023, 51872030), Joint R&D Plan of Hongkong, Macao, Taiwan and Beijing (No. Z191100001619002), the Fundamental Research

Funds for the Central Universities (No. 2017CX01003), and the Beijing Institute of Technology Research Fund Program for Young Scholars.

Supplementary materials

Supplementary material associated with this article can be found, in the online version, at doi:10.1016/j.cclet.2021.10.088.

References

[1] S. Bai, N. Zhang, C. Gao, J. Y, Nano Energy 53 (2018) 296–336.
[2] Q. Wang, K. Domen, Chem. Rev. 120 (2020) 919–985.
[3] C. Xie, D. Yan, H. Li, et al., ACS Catal. 10 (2020) 11082–11098.
[4] L. Fu, R. Wang, C.X. Zhao, et al., Chem. Eng. J. 414 (2021) 128857.
[5] R. Wang, C.Z. He, W.X. Chen, C.X. Zhao, J.R. Huo, Chin. Chem. Lett. 32 (2021) 3821–3824.
[6] Y. Liu, M.S. M.olokeev, Z. G. Xia, Energy. Mater. Adv. 9 (2021) 2585274.
[7] J.H. Chang, H.J. Lee, S. Rhee, et al., Energy. Mater. Adv. 10 (2021) 3245731.
[8] J. Di, J. Xiong, H.M. Li, Z. Liu, Adv. Mater. 30 (2018) 1704548.
[9] J. Xiong, J. Di, J.X. Xia, W.S. Zhu, H.M. Li, Adv. Funct. Mater. 28 (2018) 1801983.
[10] Y.W. Teh, C.M. Fung, M.K.T. Chee, et al., Materials Today 43 (2020) 198–212.
[11] Y.F. Sun, S. Gao, F.C. Lei, Y. Xie, Chem. Soc. Rev. 44 (2015) 623–636.
[12] H.Q. Yang, Q.Q. Chen, F.L. Liu, R. Shi, Y. Chen, Chin. Chem. Lett. 32 (2021) 676–680.
[13] Y.Y. Okamoto, S. Ida, J. Hyodo, H. Hagiwara, T. Ishihara, J. Am. Chem. Soc. 133 (2011) 18034–18037.
[14] F.C. Lei, L. Zhang, Y.F. Sun, et al., Angew. Chem. Int. Ed. 54 (2015) 9266–9270.
[15] J.M. Li, D. Yi, F. Zhan, et al., Appl. Catal. B: Environ. 271 (2020) 118925.
[16] Y.R. Li, Z.W. Wang, T. Xia, et al., Adv. Mater. 28 (2016) 6959–6965.
[17] A. Agrawal, S.H. Cho, O. Zandi, et al., Chem. Rev. 118 (2018) 3121–3207.
[18] S.Y. Han, X. Qin, Z.F. An, et al., Nat. Commun. 7 (2016) 13059.
[19] Z.K. Liu, Y.X. Zhong, I. Shafei, et al., Nat. Commun. 10 (2019) 1394.
[20] T.R. Gordon, T. Paik, D.R. Klein, et al., Nano Lett. 13 (2013) 2857–2863.
[21] A. Sahu, M.S. Kang, A. Kompch, et al., Nano Lett. 12 (2012) 2587–2594.
[22] M. Sharma, M. Olutas, A. Yeltik, et al., Chem. Mater. 30 (2018) 3265–3275.
[23] L.M. Yang, K.E. Knowles, A. Gopalan, et al., Chem. Mater. 28 (2016) 7375–7384.
[24] M. Sytnyk, R. Kirchschlager, M.I. Bodnarchuk, et al., Nano Lett. 13 (2013) 586–593.
[25] P. Chakraborty, Y. Jin, C.J. Barrows, S.T. Dunham, D.R. Gamelin, J. Am. Chem. Soc. 138 (2016) 12885–12893.
[26] S. Lentijo-Mozo, D. Deiana, E. Sogne, A. Casu, A. Falqui, Chem. Mater. 30 (2018) 8099–8112.
[27] Z.S. Luo, E. Irtem, M. Ibanez, et al., ACS Appl. Mater. Interfaces 8 (2016) 17435–17444.
[28] Z.H. Zhao, X.Q. Chi, L.J. Yang, et al., Chem. Mater. 28 (2016) 3497–3506.
[29] A.G. Dong, X.C. Ye, J. Chen, et al., J. Am. Chem. Soc. 133 (2011) 998–1006.
[30] M. Qiao, J. Liu, Y. Wang, Y. Li, Z. Chen, J. Am. Chem. Soc. 140 (2018) 12256–12262.
[31] X.M. Zhang, J. Liu, E.H. Zhang, et al., Chem. Commun. 56 (2020) 5504–5507.
[32] J.F. Shen, Y.M. He, J.J. Wu, et al., Nano Lett. 15 (2015) 5449–5454.
[33] L. De Trizio, L. Manna, Chem. Rev. 116 (2016) 10852–10887.
[34] S. Gupta, S.V. Kershaw, A.L. Rogach, Adv. Mater. 25 (2013) 6923–6943.
[35] J. Liu, J.T. Zhang, Chem. Rev. 120 (2020) 2123-217.
[36] L.X. Meng, S.Y. Wang, F.R. Cao, et al., Angew. Chem. Int. Ed. 58 (2019) 6761–6765.
[37] H.H. Liu, K.F. Tian, J.Q. Ning, et al., ACS Catal. 9 (2019) 1211–1219.
[38] N. Zhang, A. Jalil, D.X. Wu, et al., J. Am. Chem. Soc. 140 (2018) 9434–9443.
[39] R.R. Pan, M. Hu, J. Liu, et al., Nano Lett. 21 (2021) 6228–6236.
[40] D. Parobek, B.J. Roman, Y. Dong, et al., Nano Lett. 16 (2016) 7376–7380.
[41] A. De, N. Mondal, A. Samanta, Nanoscale 9 (2017) 16722–16727.
[42] Z.Y. Zhang, Q.Y. Wu, G. Johnson, et al., J. Am. Chem. Soc. 141 (2019) 16548–16552.
[43] D.M. Zhao, C.L. Dong, B. Wang, et al., Adv. Mater. 31 (2019) 1903545.
[44] J. Wirth, R. Neumann, M. Antonietti, P. Saalfrank, Phys. Chem. Chem. Phys. 16 (2014) 15917–15926.
[45] Y. Wang, C. Zhu, G. Zuo, Y. Guo, W. Xiao, et al., Appl. Catal. B: Environ. 278 (2020) 119298.
[46] M.S. Xie, F.F. Dai, X.Y. Dang, et al., Angew. Chem. Int. Ed. 60 (2021) 14370–14375.
[47] S.Y. Dong, J.Y. Sun, Y.K. Li, et al., Appl. Catal. B: Environ. 144 (2014) 386–393.
[48] H.B. Ammar, Ultrason. Sonochem. 33 (2016) 164–169.